$La_2O_3Mn_2Se_2$: A correlated insulating layered *d*-wave altermagnet

Chao-Chun Wei,[1] Xiaoyin Li,[1] Sabrina Hatt,[2] Xudong Huai,[3] Jue Liu,[4] Birender Singh,[5] Kyung-Mo Kim,[5] Rafael M. Fernandes,[6] Paul Cardon,[1] Liuyan Zhao,[7] Thao T. Tran,[3] Benjamin A. Frandsen,[2] Kenneth S. Burch,[5] Feng Liu,[1] and Huiwen Ji[1,*]

[1]*Department of Materials Science and Engineering, University of Utah, Salt Lake City, Utah 84112, USA*
[2]*Department of Physics and Astronomy, Brigham Young University, Provo, Utah 84602, USA*
[3]*Department of Chemistry, Clemson University, Clemson, South Carolina 29634, USA*
[4]*Neutron Sciences Division, Oak Ridge National Laboratory, Oak Ridge, Tennessee 37831, USA*
[5]*Department of Physics, Boston College, Chestnut Hill, Massachusetts 02467, USA*
[6]*Department of Physics, University of Illinois Urbana-Champaign, Urbana, Illinois 61801, USA*
[7]*Department of Physics, University of Michigan, Ann Arbor, Michigan 48109, USA*

(Received 16 October 2024; accepted 28 January 2025; published 11 February 2025; corrected 25 February 2025)

Altermagnets represent a new class of magnetic phases without net magnetization, invariant under a combination of rotation and time reversal. Unlike conventional collinear antiferromagnets (AFM), altermagnets could lead to new correlated states and important material properties deriving from their nonrelativistic spin-split band structure. Indeed, they serve as the magnetic analogue of unconventional superconductors and can yield spin-polarized electrical currents in the absence of external magnetic fields, making them promising candidates for next-generation spintronics. Here, we report altermagnetism in the correlated insulator, magnetically ordered tetragonal oxychalcogenide, $La_2O_3Mn_2Se_2$. Symmetry analysis reveals a $d_{x^2-y^2}$-wave-like spin-momentum locking arising from the Mn_2O Lieb lattice, supported by density functional theory (DFT) calculations. Magnetic measurements confirm the AFM transition below ∼166 K while neutron pair distribution function analysis reveals a 2D short-range magnetic order that persists above the Néel temperature. Single crystals are grown and characterized using x-ray diffraction, optical and electron microscopy, and micro-Raman spectroscopy to confirm the crystal structure, stoichiometry, and uniformity. Our findings establish $La_2O_3Mn_2Se_2$ as a model altermagnetic system realized on a Lieb lattice.

DOI: 10.1103/PhysRevMaterials.9.024402

I. INTRODUCTION

Magnetic memory and spintronics have historically relied on ferromagnetism (FM) for straightforward implementations in devices [1,2]. Over the past decade, several paradigms of antiferromagnetic (AFM) spintronics have been demonstrated, offering advantages such as zero stray fields, robustness against external perturbations, potential for miniaturization, and ultrafast switching dynamics [3–6]. However, the spin degeneracy enforced throughout the band structure and the need to couple the magnetic response to electric fields have limited the potential applicability of most AFM materials. To overcome these challenges, the community has focused on materials with strong spin-orbit coupling (SOC) [7–9], which requires heavy elements and complex magnetic orders that limit their widespread adoption.

Recent progress in the theoretical classification of spin groups, where SOC is absent, has identified a new class of magnetic states called altermagnets, which exhibit $\boldsymbol{k}$-dependent spin polarization yet zero net magnetization [10,11]. Such a nonrelativistic spin splitting is a consequence of the fact that the magnetic configuration is invariant under a combination of time reversal, which flips the magnetic moments, and real-space rotations, which can be proper, improper, or accompanied by half-translations (i.e., a nonsymmorphic operation) [12]. Altermagnets are promising for compact and high-speed spintronics, and their material choices are no longer restricted to heavy-metal compounds since the spin splitting is not enforced by SOC [10,13,14]. Emerging properties such as the anomalous Hall effect [11,15,16], current polarization [17,18], tunneling and giant magnetoresistance have been predicted based on the symmetries of the spin density in the crystal structure [19]. Altermagnets are divided into *d*-, *g*-, and *i*-wave types, based on the number of nodal planes (k-space planes on which bands are spin degenerate) between spin-split bands in momentum space [10,12]. As such these materials form a long-sought magnetic analogue to the higher-momentum, unconventional superconducting states known for decades [20]. To date, numerous materials have been predicted to be altermagnetic [21–25], and direct experimental evidence has been reported in *g*-wave type MnTe and CrSb [26,27], while the status of RuO_2 (a predicted *d*-wave type altermagnet) remains unsettled [28–32].

An interesting open question is the interplay between altermagnetism and strongly correlated materials, which can be investigated in Mott insulating or correlated metallic

*Contact author: huiwen.ji@utah.edu

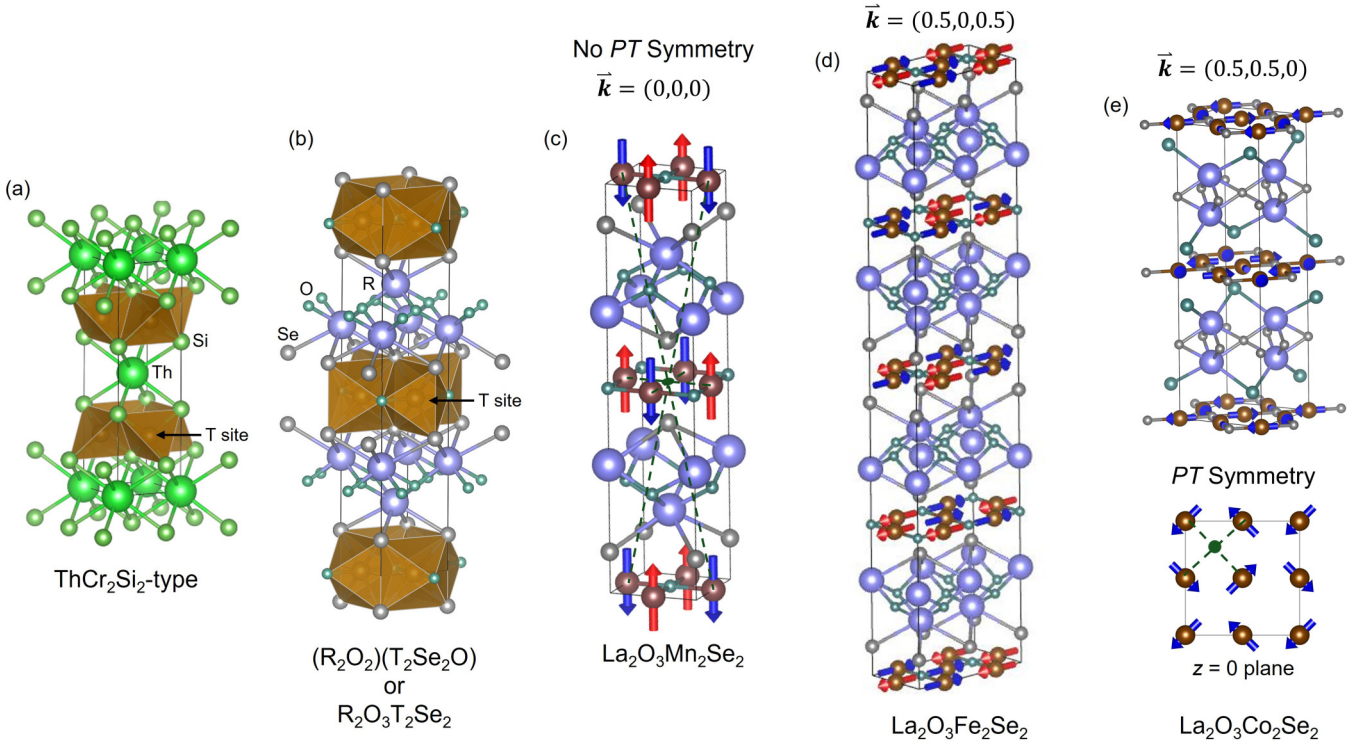

FIG. 1. Atomic crystal structures of (a) $ThCr_2Si_2$ and (b) $(R_2O_2)(T_2Se_2O)$ and magnetic structures of (c) $La_2O_3Mn_2Se_2$, (d) $La_2O_3Fe_2Se_2$, and (e) $La_2O_3Co_2Se_2$. Blue/red arrows in (c)–(e) point at the directions of the compensating moments, while the inversion centers are highlighted by green-colored dots in (c) and (e). Representative pairs of atoms connected by inversion are linked by dashed lines in (c) and (e).

materials, whose crystalline symmetries "convert" the conventional antiferromagnetic ground state into an altermagnetic state. To identify new types of correlated material candidates with d-wave altermagnetism, we turn to the layered $R_2O_3T_2Ch_2$ (R = rare earth, T = transition metal, Ch = chalcogen) family [33–36]. This family has been studied in the past decades for its structural resemblances to the layered $ThCr_2Si_2$ family (122-type) [Fig. 1(a)] [37–39], in which Fe-based superconductors were discovered (for a recent review, see Ref. [40]). The crystal structure of these compounds [Fig. 1(b)] adopts 2D square arrays of transition metals (TMs), such as Fe, Mn, Co that are octahedrally coordinated by four chalcogen and two O atoms in a face-sharing network. As a result, the Mn_2O plane forms a Lieb lattice, which has been widely studied theoretically as a simple realization of altermagnetic order [41–43]. Indeed, the resultant fourfold rotation symmetry connecting the two TM sublattices provides an ideal platform to realize d-wave type altermagnets. Unlike most other altermagnetic candidates, rotation relating the time-reversed spin states involves two different anion species, i.e., O, Se. These materials are predominantly magnetically ordered with electrically insulating properties regardless of the TM species, which has been attributed to a Mott insulating or orbital-selective Mott state [34,35,44,45]. Indeed, resistivity measurements show insulating behavior already in the paramagnetic phase, whereas DFT calculations generally predict a metallic phase [59]. In addition, the mixed-anion coordination environments around TMs can lower local crystal symmetry, enhance local anisotropy [46], and, with specific AFM order, might induce altermagnetism.

In this paper, we revisit this structure family and report d-wave type altermagnetism predicted in the layered compound $La_2O_3Mn_2Se_2$ (LOMSO). The compound was initially discovered by Ni *et al.* and its magnetic structure was identified through powder neutron diffraction [47]. Here, symmetry analysis based on its reported G-type $\boldsymbol{k} = (0, 0, 0)$ magnetic ground-state order (magnetic space group $I4'/mm'm$) indicates the breaking of certain symmetries and the subsequent rise of d-wave spin momentum locking. The prediction is supported by density-functional theory (DFT) calculations, which further show that adding SOC modifies the electronic structure by lifting spin degeneracy at nodal planes and converting them into symmetry-protected nodal lines. Magnetic measurements confirm the AFM ground state and a competing FM component. Neutron pair distribution function (PDF) analysis reveals a 2D short-range intraplanar AFM order that persists even above the magnetic ordering temperature. Finally, single-crystal samples of several hundred micrometers were grown, and their stoichiometry, uniformity, and layered crystal structure were confirmed through single crystal x-ray diffraction, optical and electron microscopy, and micro-Raman spectroscopy.

II. METHODS

La_2O_3 was prepared from heating $La(OH)_3$ (Sigma Aldrich, 99.9% trace metals basis) at 900 °C for 48 hours. Manganese powder (Thermo Scientific, 99.95%), selenium shot (Thermo Scientific, 99.999%), and La_2O_3 were then combined in a stoichiometric molar ratio of 2:2:1, ground,

pelletized, and sealed in a quartz tube. The mixture was first heated to 700 °C, followed by regrinding, and a second heat treatment at 950 °C for 48 hours. To prepare single crystals, the synthesized LOMSO powder was pelletized and placed in a high-temperature tube furnace with an argon flow. The temperature was increased at a rate of 3 °C/ min to 1000 °C, then at 1 °C/ min to 1200 °C, and held for 24 hours. The furnace was then cooled to 1000 °C at a rate of 1 °C/ min over 18 hours, followed by cooling to room temperature at 3 °C/ min.

A STOE STADI P x-ray diffractometer was used in transmission geometry to collect powder diffraction data with a Mo anode with Kα1 radiation ($\lambda = 0.7094$ Å), a Ge (111) curved monochromator, and a Dectris MYTHEN2 detector. Data were collected at room temperature in static mode across the 2θ angle range of 2° to 60° on LOMSO powder over 11.5 hours. Structural refinement was done with the GSAS-II software package. VESTA was used to visualize crystal structures.

Neutron pair distribution function (PDF) measurements were performed on the NOMAD instrument at the Spallation Neutron Source. The PDF method involves Fourier transforming the total scattering pattern (including both Bragg scattering from long-range-ordered correlations and diffuse scattering from short-range correlations) to reveal the local structure in real space [48]. When PDF experiments are performed on magnetic materials using a neutron beam, the magnetic correlations present in the material produce the magnetic PDF (mPDF) as an additional component of the total PDF data [49,50], providing insight into both the atomic and magnetic correlations on local length scales. In this paper, the sample was contained in a 3-mm diameter thin quartz capillary, and an argon cryoblower was used to control the sample temperature. Data were collected at 100 K, 200 K, 300 K, and 400 K. Two 24-min scans were collected at each temperature point and summed together to improve the statistics. Neutron scattering signals were background subtracted, and the obtained intensity was normalized to the scattering signal from a 6-mm vanadium rod to correct for detector efficiency. Using the standard protocols at the beamline, the raw diffraction data were reduced to the total scattering structure function, which was then transformed into the PDF with a maximum momentum transfer of 30 $Å^{-1}$. Combined magnetic and atomic PDF corefinements were performed using the diffpy.mpdf and diffpy.srfit packages [51,52], part of the DiffPy suite of Python-based diffraction software.

Scanning electron microscopy (SEM) (FEI TENEO) was used for imaging with a secondary electron detector and a 20-kV high-voltage beam, at a magnification of 1200× and a working distance of 10.5 mm. Energy dispersive spectroscopy (EDS) uses EDAX Octane Elect SDD. The working distance and voltage are the same as SEM. KEYENCE VHX-500 was used for optical microscopy (OM) imaging.

Temperature- and field-dependent magnetization measurements were performed in a Quantum Design Physical Properties Measurement System (PPMS) using a vibrating-sample magnetometer option. Magnetic susceptibility was approximated by normalizing magnetization by the field applied.

First-principles calculations of LOMSO were performed based on density-functional theory (DFT) as implemented in the Vienna *Ab initio* Simulation Package (VASP) [53]. The projector augmented wave method was used to describe the interactions between core-valence electrons [54], and the Perdew-Burke-Ernzerhof-type generalized gradient approximation was employed for the exchange-correlation functional [55]. The energy cutoff for the plane-wave expansion was set to 520 eV, and the Brillouin zone was sampled by a $13\times13\times3$ Monkhorst-Pack mesh [56]. To describe the strongly correlated $3d$ electrons of Mn, the rotationally invariant DFT+U scheme was implemented [57], using an effective U value of 4 eV based on a similar choice made for MnO [58]. The lattice constants and atomic positions were fully relaxed to obtain the computationally optimized structure. The obtained optimal lattice constants are $a = b = 4.16$ Å, $c = 19.17$ Å, and $\alpha = \beta = \gamma = 90°$, the difference between which and the previously reported experimental values near room temperature, i.e., $a = 4.14$ Å, $c = 18.85$ Å, are within 1% [47,59]. Convergence criteria for energy and force were set to 10^{-5} eV and –0.001 eV/Å, respectively.

Micro-Raman spectroscopy was performed using a custom-built system with a 532-nm excitation laser and 1-μm spot size [60,61]. The incident and scattered polarization were controlled using motorized half-waveplates with spectra collected every fifteen degrees from 0 to 360. The incident power was kept below 0.1 mW, and we confirmed the absence of heating by doubling the integration power and reducing the power by half did not affect the spectra. A total of 10 different single crystals were measured, as well as spectra acquired from multiple spots on three different crystals. The spectra were all identical, and the polarization dependence was also highly consistent across crystals.

III. RESULTS AND DISCUSSION

Figure 1(b) shows the crystal structure of $R_2O_3T_2Se_2$. The (T_2Se_2O) octahedra layers have a square pattern and are separated by the (R_2O_2) spacer layers. Across a (R_2O_2) spacer layer, the two nearby T_2Se_2O layers are offset in plane by $\frac{1}{2}\,\boldsymbol{a} + \frac{1}{2}\,\boldsymbol{b}$. In this family, the presence or absence of altermagnetism depends on the magnetic configuration, which in turn depends on the TM. For example, the magnetic structure of the more widely studied $La_2O_3Fe_2Se_2$ adopts in-plane moments and a zig-zag type AFM order that doubles the unit cell along $\boldsymbol{a}$ and $\boldsymbol{c}$ axes, giving rise to a nonzero propagation vector $\boldsymbol{k} = (\frac{1}{2}, 0, \frac{1}{2})$, as shown in Fig. 1(d) [62]. The magnetic structure thus hosts τT symmetry (where τ is translation and T is time reversal) and does not qualify as an altermagnet, being instead an AFM. The Co analogue, $La_2Co_2O_3Se_2$ [Fig. 1(e)], develops a coplanar noncollinear magnetic structure below ∼217 K, wherein nearby Co moments are orthogonal with a nonzero $\boldsymbol{k} = (\frac{1}{2}, \frac{1}{2}, 0)$ [63]. The magnetic structure thus preserves both PT [one inversion center highlighted in the lower panel of Fig. 1(e)] and τT symmetry and does not lead to altermagnetism.

The Mn variant, which is relatively less explored with only one report on its magnetic structure through neutron diffraction, on the other hand, might be altermagnetic based on symmetry analysis. The G-type order, as shown in Fig. 1(c)

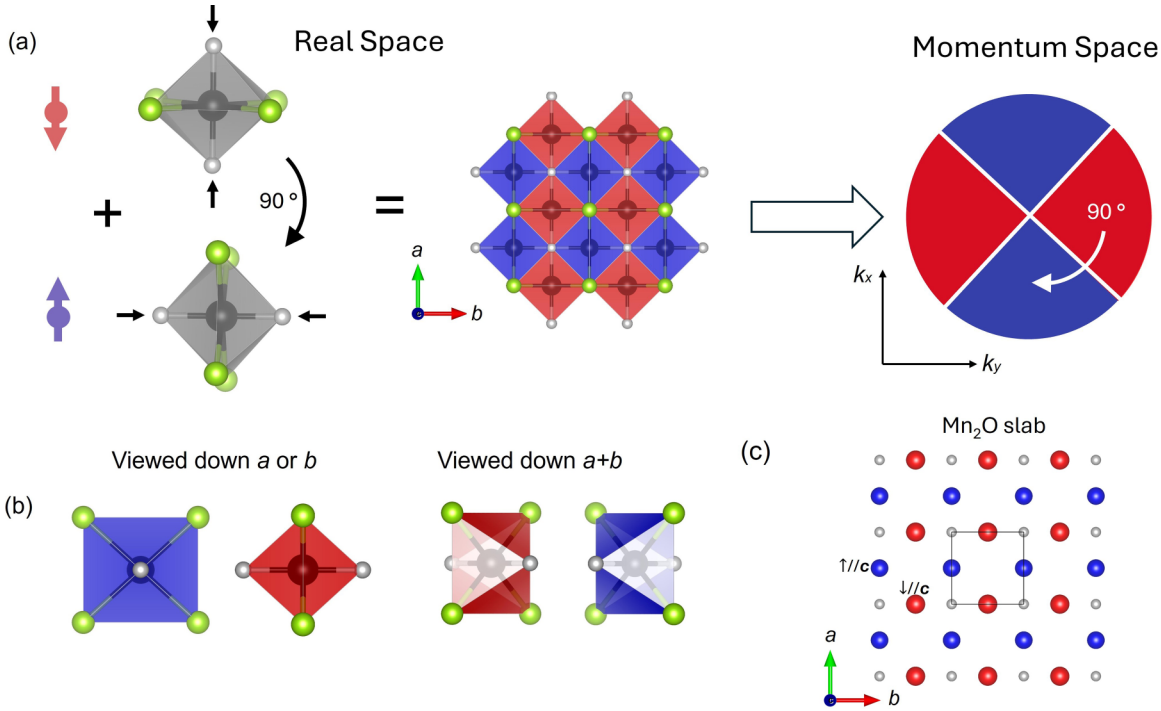

FIG. 2. Origin of d-wave altermagnetism in LOMSO. (a) The fourfold or 90° rotation between the opposite-spin sublattices (in red and blue) in real space yields d-wave type spin-momentum locking in momentum space. The anisotropy directions in $MnSe_4O_2$ octahedra are highlighted. The blue and red blocks in momentum space indicate spin-momentum locking without SOC, while the spin-degenerate nodal planes are depicted using white lines. (b) Inspection of the Mn_2Se_2O octahedra down a (or b) and $a+b$ directions sheds light upon the spin-splitting direction. (c) The Mn_2O slab with spin-up, -down Mn and O atoms in blue, red, and white, respectively.

for $La_2O_3Mn_2Se_2$ (LOMSO) [47], features opposite spins in the nearest-neighbor TMs and a checkerboard-type magnetic moment pattern that does not break translational symmetry. Two key criteria for altermagnet identification are met here: (i) The absence of parity-time reversal (PT) symmetry [10]. This is evident in the crystal structure, where pairs of atoms connected by inversion symmetry (marked by dashed lines) exhibit parallel magnetic moments, indicating the breaking of PT symmetry. (ii) The lack of translation-time reversal (τT). The magnetic propagation vector $\boldsymbol{k} = (0, 0, 0)$ suggested from previous neutron scattering studies rules out a magnetic supercell, automatically ensuring the absence of τT symmetry. The two sublattices are instead connected by fourfold rotation, which is the defining property of altermagnetism. Even in the absence of SOC, a highly desired d-wave type spin-momentum locking is predicted with two orthogonal spin-degenerate nodal planes parallel to the fourfold rotation axis ($\boldsymbol{c}$ axis).

As shown in Fig. 2(a), the mixed anion coordination environments create local anisotropy, i.e., two shorter Mn-O bonds and four long Mn-Se bonds. The two nearby $MnSe_4O_2$ octahedra are related by a fourfold or 90° rotation and have opposite moments. Because the two Mn atoms in each unit cell are located at (1/2, 0, 0) and (0, 1/2, 0), the spin splitting is maximized along the main axes and vanishes along the diagonals. This can also be seen by comparing the two opposite-spin $MnSe_4O_2$ octahedra from a view down the a or b axis [Fig. 2(b)], where they look different, and from a view down the $a + b$ axis [Fig. 2(c)], where they look identical. Thus, accordingly, without SOC, the bands with opposite spins are split except along the two vertical nodal planes $k_x = \pm k_y$ (i.e., parallel to the $\Gamma-M$ directions), as shown in Fig. 2(a) on the right. This implies that the magnetically ordered state of LOMSO is altermagnetic, as it is invariant under a combination of a fourfold rotation and time reversal, corresponding to the $[C_2||C_{4z}]$ symmetry operation in spin-group language [10]. Since the nodes along which the electronic bands are spin-degenerate correspond to the planes $k_x = \pm k_y$, which coincide with the directions for which the $d_{x^2-y^2}$ form factor vanishes, we identify the order parameter of LOMSO as a $d_{x^2-y^2}$-wave altermagnet [10,41], for which the momentum-space spin density behaves as $\boldsymbol{S_k} \propto (k_x^2 - k_y^2)\boldsymbol{\sigma}$. Note that this symmetry is distinct from the more widely discussed d-wave altermagnetic rutiles, which have a d_{xy}-wave character with nodal planes along $k_x = 0$ and $k_y = 0$ (i.e., parallel to the $\Gamma-X$ and $\Gamma-Y$ directions). As we explain below, the $d_{x^2-y^2}$-wave altermagnetic order parameter is perfectly consistent with the magnetic space group assigned for LOMSO in the literature. Interestingly, the Mn_2O plane, highlighted in Fig. 2(c), consists of a realization of the Lieb lattice, which has been invoked in the literature as a model lattice to investigate altermagnetism [41–43]. Thus, LOMSO is a model altermagnetic system in which theoretical predictions of this simple model could be tested.

To confirm the above symmetry analysis, first-principles calculations were carried out to obtain the real-space spin-density distribution and the reciprocal momentum space band structure. The results in Fig. 3(a) show the anisotropic spin

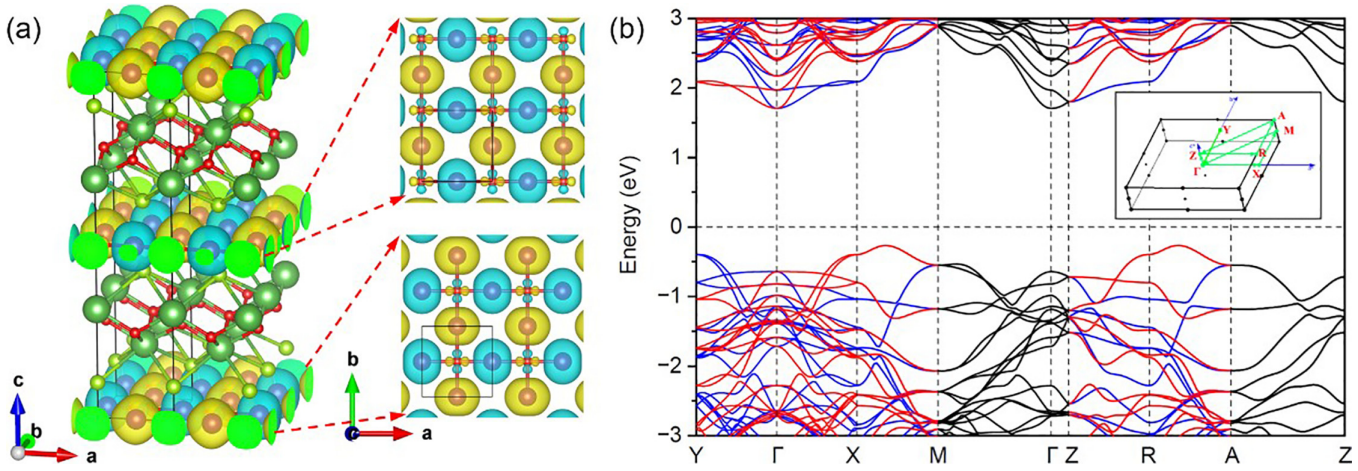

FIG. 3. (a) Perspective (left panel) and top (right panels) views of the real-space spin-density distribution of $La_2O_3Mn_2Se_2$. Isosurfaces of up- and down-spin densities are in yellow and blue, respectively. (b) Spin-projected band structure of $La_2O_3Mn_2Se_2$ without SOC. Red and blue lines represent the spin-up and -down polarized bands. The degenerate bands with compensated spin components are plotted as black-solid lines. The first Brillouin zone is included as an inset.

density distribution in the opposite-spin Mn sublattices, consistent with our analysis in Fig. 2. Figure 3(b) plots the electronic band structure, in which the blue and red dispersions refer to the spin-up and -down polarized bands, while the black-colored bands are spin degenerate. The first Brillouin zone of the magnetic structure is shown on the right. SOC was first purposely left out because altermagnetism is not a relativistic effect and does not rely on SOC to emerge. In the absence of SOC, LOMSO indeed exhibits a momentum-dependent spin splitting, which implies an altermagnetic order. This behavior contrasts with that of conventional FMs, where spin splitting is typically uniform across the entire Brillouin zone, and collinear AFMs, which show no net spin splitting owing to the compensating magnetic moments. Significant splitting as large as nearly 0.7 eV is observed between the spin-up and spin-down channels along the $\Gamma-X(Y)$, and reverses its polarization when rotating from $\Gamma-X$ to $\Gamma-Y$, confirming our prediction of a $d_{x^2-y^2}$-wave modulation of the spin splitting. A gap >1.5 eV is also observed, which is consistent with the insulating nature generally assigned to this class of materials as well as the green color of the as-synthesized powder. The gap size is affected by the effective U parameter: a larger U leads to a larger gap (Fig. S1 within the Supplemental Material [64]). Based on DFT calculations, unlike the Fe analogue, LOMSO displays a G-type compensated magnetic state even in the limit of $U = 0$. Indeed, as shown in Table I within the Supplemental Material [64], regardless of the functional used, the compensated magnetic state is always the ground state and much lower in energy compared to the FM or the nonmagnetic state. While the band structure is gapped by the magnetic order even when U is set to zero, the nonmagnetic state displays a metallic electronic structure (Fig. S2 within the Supplemental Material [64]). Previous resistivity measurements above the magnetic transition found insulating behavior up to the highest temperatures probed [59], indicating that this material, like the other TM members of the family, is likely a Mott insulator.

The introduction of SOC modifies the electronic structure, particularly by lifting the spin degeneracy at the nodal planes in the Brillouin zone, which without SOC are parallel to $\Gamma-M$ and $\Gamma-Z$. In the presence of SOC, the direction of the magnetic moments matters [41], impacting the momentum-dependent spin-density, which, without SOC, is given by $\boldsymbol{S_k} \propto (k_x^2-k_y^2)\boldsymbol{\sigma}$. When the moments are oriented along the $\boldsymbol{c}$axis, which is the case for LOMSO according to Ref [47] and as our neutron experiment also confirmed below, the altermagnetic order parameter transforms as the B_{2g}^- irreducible representation (irrep) of the tetragonal point group D_{4h}, following the

TABLE I. Crystal structure refinement data and parameters from SXRD.

Space group type	I4/mmm
Crystal system	tetragonal
Formula (refined)	$La_2Mn_2Se_2O_3$
a (Å)	4.12740(7)
c (Å)	18.8057(5)
V (Å^3)	320.363(14)
Z	2
Temperature	100(2) K
Crystal Size (um)	100, 70, 20
λ	0.71073
μ (mm^{-1})	28.191
Absorption Correction	Gaussian
T_{min}, T_{max}	0.165, 0.602
Reflections measured, unique, used	4028, 526, 526
Resolution (d_{min}, $2\theta_{max}$)	0.442, 107.13
$(hkl)_{max}$	(–9,8), (–9,9), (–42, 35)
Parameters	15
Method of refinement	Shelx, $\|F^2\|$
wR_2 (all)	0.0361
R_1 (all)	0.0180
GOF	1.174
F_{000}	512
Max residual density	2.655,–2.519 (REM highest difference peak)
CSD code	2408123

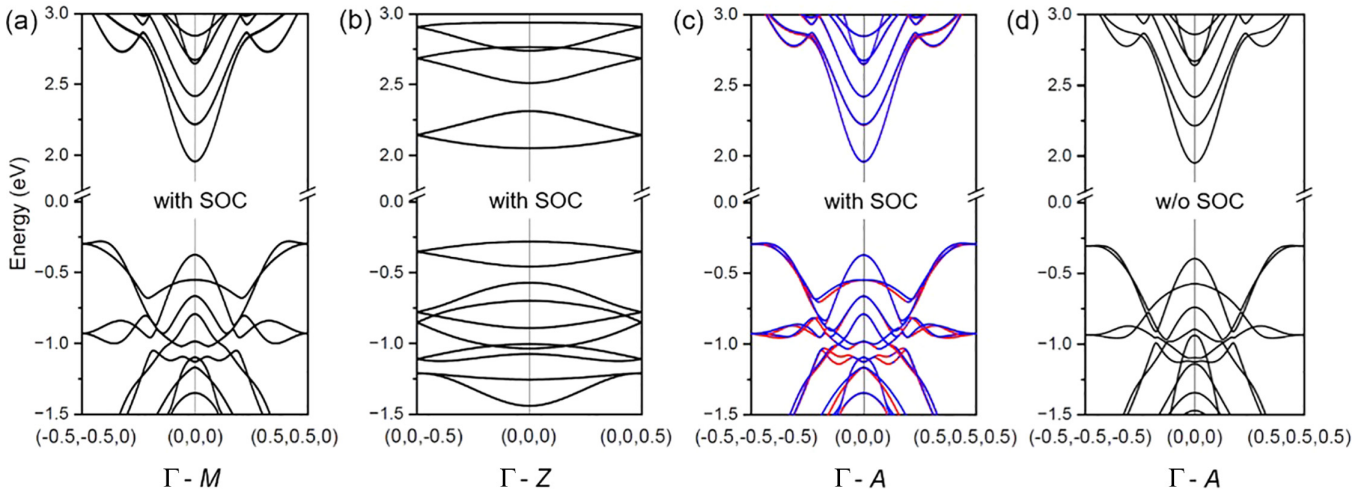

FIG. 4. DFT electronic structure calculations (a)–(c) with SOC included along the Γ-M, Γ-Z, and Γ-A path, and without SOC along Γ-A. The blue and red bands are spin split, while the black ones are spin degenerate. This is consistent with the classification of Ref. [65] for a $d_{x^2-y^2}$-wave altermagnet, according to which the $k_x = \pm k_y$ nodal planes become, in the presence of SOC, the nodal lines $k_x = k_y$, $k_z = 0$; $k_x = -k_y$, $k_z = 0$; $k_x = k_y = 0$.

notation of Ref. [65] (the minus superscript indicates that the quantity is odd under time reversal). Indeed, the B_{2g}^- irrep transforms as a magnetic moment oriented along the z direction (A_{2g}^-) multiplied by a $d_{x^2-y^2}$ form factor (B_{1g}^+). In the presence of such an order parameter, the (magnetic) space group of LOMSO changes from the paramagnetic I4/mmm to the magnetic I4′/mm′m, which is the group reported in the literature for LOMSO [59]. Using the result of Ref. [65], it follows that SOC will lift the spin degeneracy everywhere on the nodal planes except along three $\boldsymbol{k}$ lines: $k_x = k_y$, $k_z = 0$; $k_x = -k_y$, $k_z = 0$; $k_x = k_y = 0$, (i.e., along k_z). The prediction is verified by DFT calculations: As shown in Figs. 4(c) and 4(d), along Γ-A, the presence of SOC induces spin splitting, whereas spin degeneracy is retained along $\Gamma-M$ and $\Gamma-Z$ [Figs. 4(a) and 4(b)]. Interestingly, the spin-splitting nodal lines are protected by crystalline mirror symmetries [65]. A main consequence is that a magnetic field perpendicular to one mirror will not gap out the nodal lines immediately.

The target compound was synthesized through a traditional solid-state calcination method. Powder x-ray diffraction was measured, and the results of Rietveld refinement are shown in Fig. 5(a). A good fit (weighted R value of 5.7%) was obtained between the observed data and the structural model with an I4/mmm space group as reported in Refs. [47,59], affirming the high purity of the sample. The compensated magnetic order in LOMSO powder was then confirmed by magnetic measurements. DC magnetic susceptibility under zero-field cooling (ZFC) and field cooling (FC) at 1000 Oe was measured from 300 K down to 2 K [Fig. 5(b)]. The magnetic transition at ∼166 K is indicated by a kink in the ZFC data and its divergence from that of FC. A small FM component was also observed below 140 K. The field-dependent ZFC susceptibility, shown in Fig. 5(c), suggests the increasing dominance of the compensated magnetic state by an external field. The more significant upturn below ∼140 K was also previously seen for the compound at ∼120 K and was attributed to the onset of spin reorientation [47]. Magnetization vs field at various temperatures is shown in Fig. 5(d). The magnetization stays mostly linear with the external field, consistent with an overall altermagnetic order. A small hysteresis loop develops as the temperature decreases to 2 K, indicating contribution from the FM component, albeit with very small magnetic moment per mole of Mn and that the altermagnetic order still dominates. Note that the 2 K hysteresis was previously observed in LOMSO and attributed to the contamination of Mn_3O_4 ($T_N = 42$ K) or intrinsic spin canting [47,59].

The origin of the competing FM component, and particularly whether it is intrinsic or extrinsic, remains unclear. For instance, the competing FM component co-existing with the dominant AFM order might lead to magnetic frustration. The signs and the relative dominance of coexisting magnetic exchange interactions in the compound can be inferred based on the observed magnetic order as well as the Goodenough-Kanamori rule. As pointed out in Ref. [47], according to the Goodenough-Kanamori rule, the close-to-90° Mn-Se-Mn (J_2) and the 180° Mn-O-Mn super-exchange (J_1) interactions between next-nearest neighbors should be FM-like and AFM-like, respectively. While the inferred FM J_2 is compatible with the G-type order, the AFM J_1 is not, which potentially gives rise to magnetic frustration [Fig. 5(f)]. The nearest-neighbor Mn-Mn direct exchange interaction J_3 should be AFM-like as inferred from the G-type ground state observed. In contrast to this intrinsic scenario, the FM component below 140 K was attributed by one report [59] to small amounts of $LaMnO_{3+\delta}$ that order ferromagnetically with divergence between FC and ZFC data below ∼140 K [66]. Regardless of the origin, the observed FM moments are very small and unlikely to significantly modify the electronic structure. In rare cases, if the FM moments are intrinsic and interlocked with the AFM moments, e.g., via the Dzyaloshinskii-Moriya interaction, then the weak FM moments can be used to control the AFM domain orientation by being susceptible to an external field [67,68].

Magnetic short-range order was previously reported based on a broad bump in neutron diffraction that corresponds to 2D magnetic order and does not completely disappear

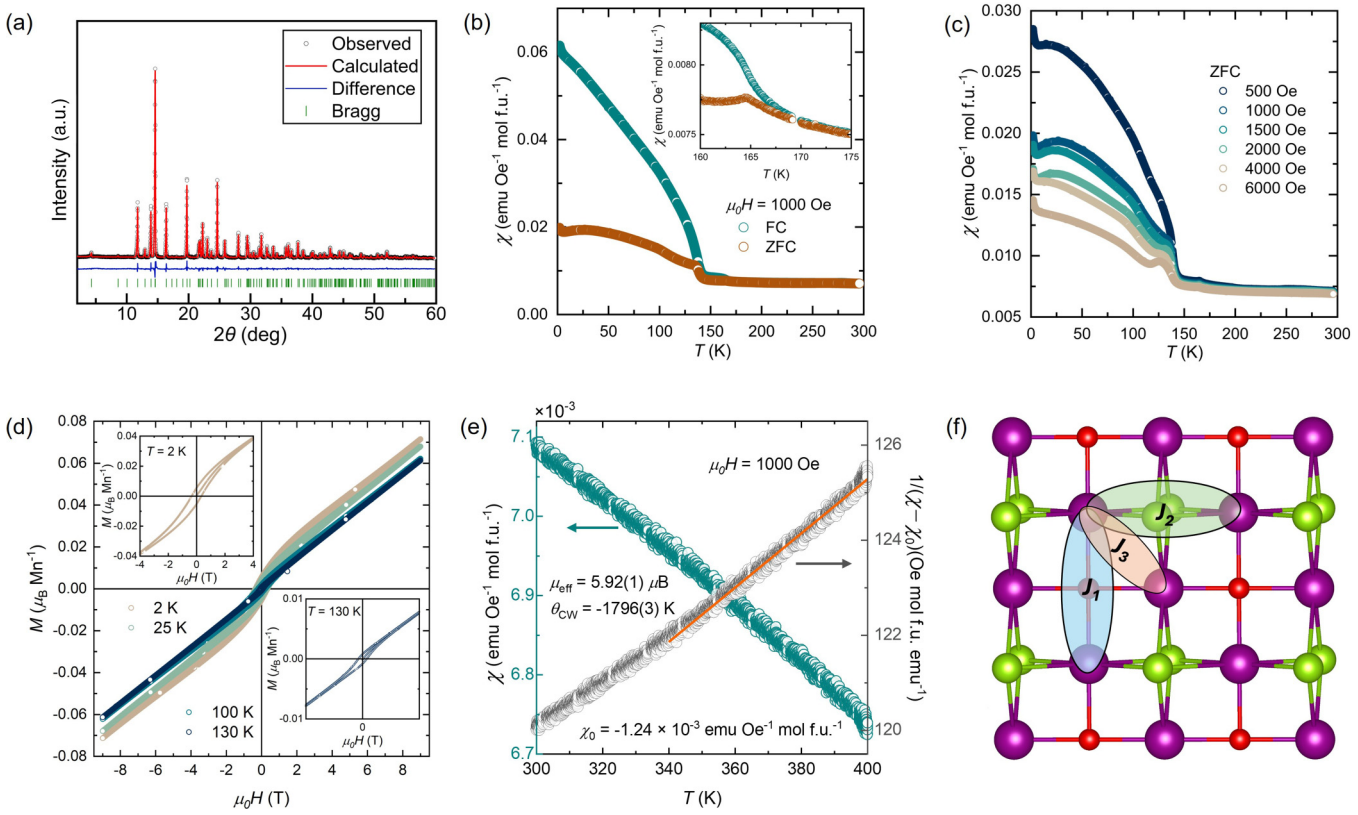

FIG. 5. Characterizations of LOMSO powder. (a) Rietveld refinement of x-ray powder diffraction pattern. (b) DC ZFC and FC magnetic susceptibility in an external magnetic field of 1000 Oe. The transition is highlighted in the zoom-in panel. (c) Magnetic susceptibility (ZFC) at various fields. (d) Magnetization vs field at various temperatures. (e) Curie-Weiss fit in a high-temperature range. (f) Schematic of coexisting exchange interactions J_1, J_2, and J_3 in the Mn_2Se_2O layer, wherein the purple, green, and red balls represent Mn, Se, and O, respectively.

even at 300 K [47]. We therefore collected additional susceptibility data between 300–400 K for a Curie-Weiss fit, which is plotted in Fig. 5(e). The significant negative $\theta_{CW} = -1796(3)$ K further indicates strong AFM-like interactions between nearest neighbors, and the effective magnetic moment of $5.92(1)\,\mu_B$/Mn is in agreement with the theoretical value for high-spin Mn^{2+}, $\sqrt{S(S+1)} = 5.92\,\mu_B$/Mn. We note that given the octahedral coordination, we would expect the T2g level of the Mn to be partially filled (i.e., d^5 state), thus the strong insulating nature and high-spin state suggest a correlated insulator of likely Mott origin.

A previous neutron diffraction study found an asymmetric broad bump underneath the magnetic (101) peak between 100 and 300 K and tentatively attributed it to possible 2D local order [47]. To better characterize the local magnetic interactions, we used a PDF method, which uses a Fourier transform of the diffraction data to highlight real-space correlations, i.e., short-range order. Neutron PDF data were collected using a time-of-flight neutron source. The PDF of LOMSO at 100 K is shown in Fig. 6(a), together with a fit to the data using a model of the atomic structure only (i.e., no magnetic component was included in the fit shown). The positions and heights of the sharp peaks in the data are well described by the fit, confirming that the accepted tetragonal crystal structure for LOMSO provides a good starting point for the PDF data. However, an inspection of the fit residual (green curve offset vertically below) reveals somewhat longer-wavelength modulations, as well as a positive bump below about 1.5 Å. These features are indicative of a magnetic component to the total PDF signal, as expected from the known long-range magnetic order that forms below 166 K in this system.

Figure 6(b) shows the magnetic component of the PDF data at each temperature, isolated by subtracting the best-fit atomic PDF calculation from the data at each temperature. To remove any temperature-independent artifacts or background signals from the data, we also subtracted the fit residual at 400 K from all other data sets. Finally, we added back in the best-fit calculated mPDF at 400 K to all lower-temperature mPDF datasets to avoid removing any real magnetic features from the lower-temperature data. At 100 K, structured features in the mPDF data persist over the full data range shown, indicative of long-range magnetic correlations. The mPDF signal at 100 K can be fit well using a two-component mPDF model that includes the published three-dimensional (3D) G-type magnetic order and a short-range-ordered, purely two-dimensional (2D) component containing the intraplanar AFM correlations [47]. Comparing the weight of the mPDF component to the total PDF signal indicates that the full $5\,\mu_B$ moment expected for Mn^{2+} spins can be accounted for by the combined 3D and 2D components. If just the 3D component is considered, the ordered moment refines to $3.3(1)\,\mu_B$, in good agreement with Ref. [47]. The combined 3D and 2D model suggests that only $\sim 3\,\mu_B$ of each local moment participates in the static long-range magnetic order, while the rest fluctuates with a short-range intralayer order [as schematically shown in Fig. 6(c)]. Within the sensitivity of the mPDF data, no

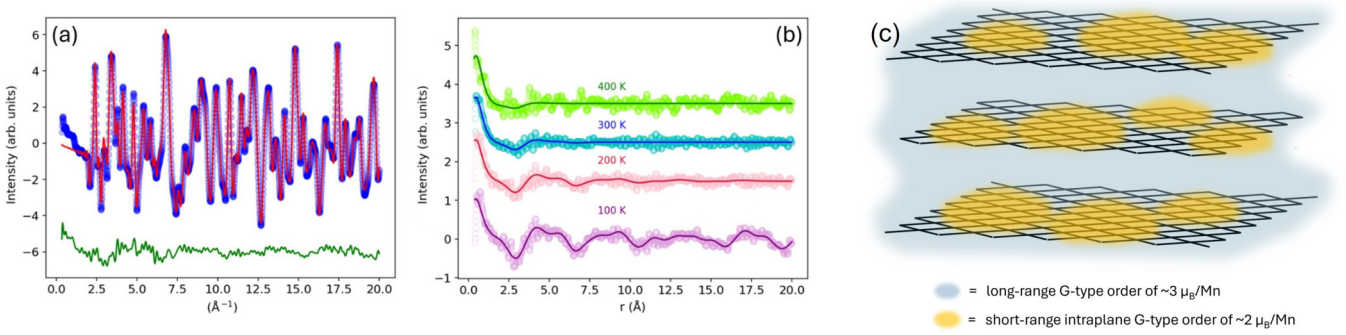

FIG. 6. (a) Atomic PDF fit to the LOMSO neutron PDF data at 100 K. The blue symbols are the total PDF data, the red curve is the best-fit atomic PDF, and the green curve is the fit residual (which contains the mPDF) offset vertically for clarity. (b) Magnetic PDF data (open symbols) and fits (solid curves) at all measured temperatures. Fits described in the main text. (c) Schematic of the 3D and 2D combined magnetic order at 100 K.

spin canting is observed at 100 K. The moment direction refines to point along the c axis for the 3D long-range-ordered component; for the 2D component, the best-fit spin direction is tilted about 45° away from the c axis, albeit with a large statistical uncertainty.

For 200 K and above, the mPDF signal is suppressed with increasing interspin distance r, confirming the presence of short-range magnetic order at these temperatures. The best fits are achieved using the purely 2D model with a finite correlation length that steadily decreases as the temperature increases. At 400 K, only the nearest-neighbor antiparallel magnetic correlation remains meaningful above the noise level in the data. The weight of the mPDF component suggests that at least $1\,\mu_B$ remains antiferromagnetically correlated between nearest-neighbor spins at 400 K, underscoring the robustness of the magnetic fluctuations in this system. A previous heat capacity measurement did not see a peak associated with the 3D magnetic transition and suggested that the magnetic entropy is nearly consumed by magnetic order already above the transition temperature [47]. As discussed later, Raman scattering at room temperature is consistent with the presence of strong short-range fluctuations. Based on the current theories [10,12,13], altermagnetism relies on long-range altermagnetic order, the 2D short-range intraplanar AFM order is thus unlikely to affect the altermagnetism.

Because the promising properties of altermagnets, especially those of the d-wave type, such as the anomalous (thermal) Hall effect and electrical current spin polarization, only arise in a coherent altermagnetic domain, single crystals are needed for future measurements and applications. LOMSO single crystals of tens of μm were previously obtained from polycrystalline pellets but the size was too small for most characterization techniques [69]. We therefore reattempted crystal growth using a similar high-temperature annealing method, which likely follows a grain growth mechanism (more details in Methods section) [70]. The pelletized powder samples after annealing appeared to have had severe evaporation and discoloration on the exposed top surface. Light green and flaky crystals can be found coating the outside of the alumina crucible on the downstream side and were indexed to unit cell dimensions close to those of α-MnSe [71]. However, translucent dark green crystals of several hundred micrometers up to sub-mm were retrieved underneath the pellet. They have a thin flaky morphology and occasional step edges on the otherwise smooth surface [see Fig. 7(a)], suggesting a lateral crystal growth mechanism.

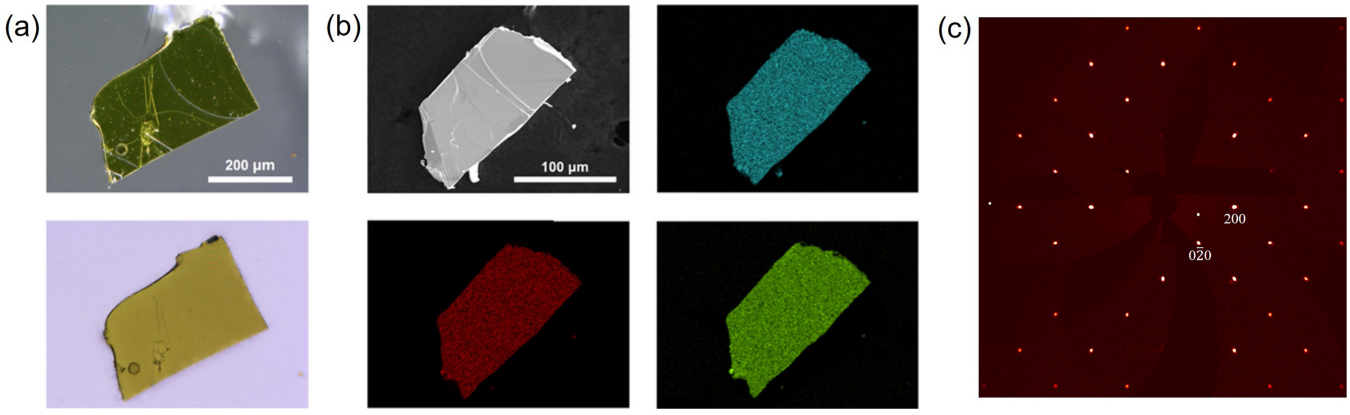

FIG. 7. (a) Ring-light (up) and transmission-light (below) optical microscope images of a LOMSO crystal. (b) SEM secondary electron image and EDS mapping of a LOMSO crystal. Light blue, red, and green represent La, Mn, and Se, respectively. (c) Measured unsymmetrized (hk0) zone of LOMSO using single-crystal x-ray diffraction.

TABLE II. Atomic sites, isotropic thermal parameters, and occupancies from SXRD.

Atom	Site	x	y	z	U_{iso} (Å^2)	Occ.
La1	La	0.5	0.5	−0.18636(2)	0.00411(3)	1
Se2	Se	0	0	−0.09997(2)	0.00554(6)	1
Mn3	Mn	0.5	0	0	0.00598(7)	1
O4	O	0	0.5	−0.25	0.0056(3)	1
O5	O	0.5	−0.5	0	0.0214(12)	1

To confirm that the crystals obtained are uniform and of the correct phase, we performed a series of analyses. Scanning electron microscopy (SEM) imaging of a typical single-crystal plate is shown in Fig. 7(b). In addition, energy-dispersive spectroscopy (EDS) shown in Fig. 7(b) confirms the uniform distribution of elements across the surface of the crystal. The EDS mapping revealed no evidence of elemental segregation or clustering, suggesting that the elements are well dispersed throughout the sample, with a composition close to the target. The crystal structure was then refined via single-crystal x-ray diffraction (SXRD) at 100 K using an XtaLAB Synergy-R high-flux rotating anode diffractometer. A representative $hk0$ zone is obtained and shown in Fig. 7(c). The indexed Bragg peaks show the characteristic tetragonal symmetry and systematic absence of Bragg peaks owing to the body-centered Bravais lattice. The refinement results are summarized in Tables I–III. Low-fitting R factors ($R_1 = 1.80\%$, $wR_2 = 3.61\%$) are obtained, indicating a good agreement between the structural model and the data. Our lattice constants refined from 100 K are $a = 4.1274$ Å, $c = 18.8057$ Å, which fall in the reported range between room temperature [47,59] and 2 K [72]. Based on the SXRD data collected, the basal plane of the crystal flake is indexed as (001), which is consistent with the layered nature of the crystal structure normal to [001].

To confirm the lattice symmetry and uniformity of the single crystals, we turned to micro-Raman spectroscopy in backscattering geometry. A typical spectrum recorded with the incident and scattered light polarizations parallel is shown in Fig. 8(a). Similar results (mode position, linewidth, and intensity) were seen in various spots on multiple crystals, indicating their uniformity and high crystal quality. The spectra taken with light propagating along the c axis revealed two strong modes (at 20 meV and 39.7 meV) and one weak mode (at 24.1 meV). Based on the crystal structure and measurement configuration, we expect to observe two modes of A_{1g} symmetry and one mode of B_{1g} symmetry. To confirm this, we measured the angle-resolved Raman response as the light

TABLE III. Anisotropic thermal parameters from SXRD.

Atom	U_{11}	U_{22}	U_{33}
La1	0.00280(4)	0.00280(4)	0.00673(6)
Se2	0.00591(8)	0.00591(8)	0.0048(2)
Mn3	0.0044(2)	0.0031(2)	0.0104(2)
O4	0.0040(5)	0.0040(5)	0.0089(9)
O5	0.0033(8)	0.0033(8)	0.0058(4)

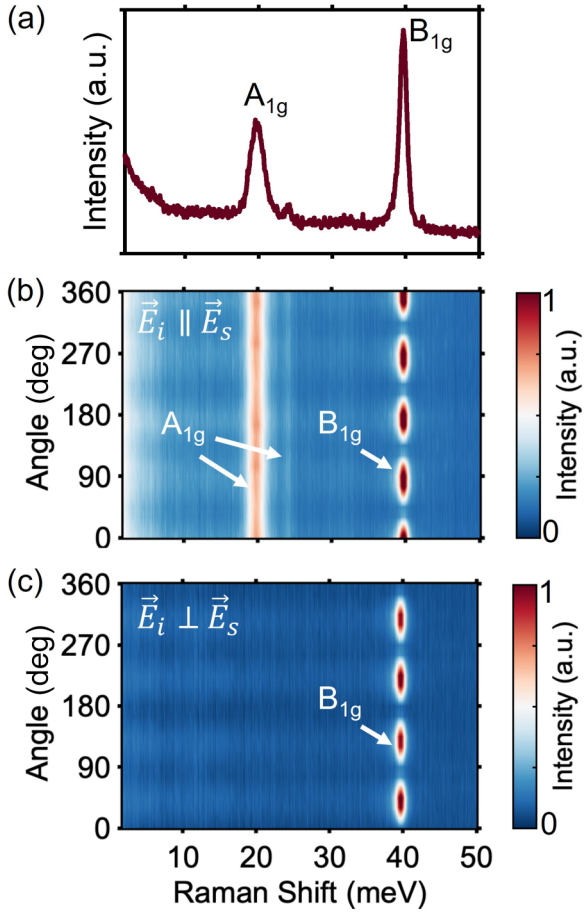

FIG. 8. (a) Raman spectra of LOMSO at 300 K in parallel (XX) polarization configuration. Color map of the angle-resolved Raman intensity at 300 K in (b) parallel (XX) and (c) crossed (XY) polarization configuration.

polarization was rotated in the plane. The results for parallel (XX) and crossed polarization (XY) of the incident and scattered light are shown in Figs. 8(b) and 8(c), respectively. As expected for the tetragonal structure with all vertical mirrors, the A_{1g} modes have an angle-independent response in XX configuration but disappear in XY. Similarly, the B_{1g} mode has a fourfold response but with the phase shifted by 45° between XX and XY. Lastly, we note the low-energy tail seen in the spectra is consistent with quasielastic scattering from strong magnetic fluctuations often seen in low-dimensional and/or frustrated magnetic systems above the ordering temperature [73,74].

As a final note, altermagnets with a d-wave spin-momentum texture can host anomalous Hall effect (AHE) as well as other anomalous transport properties [15]. However, whether AHE is allowed depends on the orientation of the Néel vector [75]. LOMSO, which has the moments aligned along the [001] direction will have a zero Hall pseudovector enforced by symmetry. If the moments can be reoriented to within the (001) plane via epitaxial strain, an external magnetic field, or by chemical doping in the transition metal or chalcogen sites (given the competing direct and indirect exchange interactions in the lattice), then a nonzero Hall vector is allowed, and its orientation will depend on the in-plane

direction of the moments. LOMSO and its analogs have large gaps which prevent electrical transport properties from being measured. A recent theoretical study has predicted the thermal Hall effect in insulating altermagnets although the effect is still contingent upon the Néel vector orientation [76].

In this context, it is interesting to contrast the magnetic ground state of LOMSO with that of the closely related compounds $R_2O_3Mn_2Se_2$ with R = Ce, Pr. According to Ref. [59], while the magnetic space group of the Ce-based compound is the same as LOMSO's (I4′/mm′m), that of the Pr-based compound is different, Im′m′m. A possible explanation for this difference is that the Pr-based compound is still altermagnetic and described by the momentum-spin density $\boldsymbol{S_k} \propto (k_x^2 - k_y^2)\boldsymbol{\sigma}$, but with the magnetic moments ($\boldsymbol{\sigma}$) pointing in-plane rather than out-of-plane. This difference, which is only relevant in the presence of SOC, makes the altermagnetic order parameter of the Pr-based compound transform as the E_g^- irreducible representation of the tetragonal group, rather than B_{2g}^- as in the case of the La- and Ce-based compounds. The E_g^- order parameter not only allows for a nonzero Hall vector and a nonzero ferromagnetic moment, but also causes an orthorhombic lattice distortion, as seen experimentally [59]. Finally, it is also illustrative to compare LOMSO with the related 122-type compound $BaMn_2As_2$, which is a member of the $ThCr_2Si_2$ (122-type) family that also has space group I4/mmm and displays a G-type magnetic order with out-of-plane moments and wavevector $\boldsymbol{k} = (0, 0, 0)$ [77]. The important difference between LOMSO and $BaMn_2As_2$ is that, in the latter, the Mn atoms on the two opposite-spin sublattices are related by inversion. As a result, the magnetic order parameter transforms as the B_{1u}^- irreducible representation, and is thus antiferromagnetic rather than altermagnetic (resulting in magnetic space group I4′/m′m′m). One way to "convert" this antiferromagnetic order into an altermagnetic order would be to apply an out-of-plane electric field (which transforms as the A_{2u}^+ irrep), for instance, by growing a very thin film on a substrate, since $B_{2g}^- = B_{1u}^- \times A_{2u}^+$; this is analogous to the strategy proposed in Ref. [42] to obtain an altermagnetic state in FeSe pnictides. The more complex crystal structure of LOMSO, however, automatically provides a proper effective field. This further illustrates the crucial role of the crystalline structure in promoting altermagnetism.

IV. CONCLUSIONS

In summary, we theoretically identified a correlated insulating d-wave altermagnet state in $La_2O_3Mn_2Se_2$, which is a member of a large structure family with flexible substitution in the spacer, transition metal, and chalcogen positions. The G-type zero wavevector magnetic ground-state order realized on the Mn_2O Lieb lattice breaks the parity-time reversal as well as the translation-time reversal symmetries but is invariant under a combination of time-reversal and fourfold rotational symmetries, thus giving rise to altermagnetism with a $d_{x^2-y^2}$-wave type spin splitting. The prediction is well aligned with DFT calculations, which show spin splitting along the $\Gamma-X(Y)$, $R-A$ and $X-M$ directions and spin degeneracy along $\Gamma-Z$ and $\Gamma-M$. Polycrystalline samples were synthesized for magnetic and neutron PDF measurements and single crystals of a several hundred micrometer size were successfully obtained through high-temperature annealing. The paper calls for future experiments such as (spin-resolved) angle-resolved photoemission spectroscopy to observe the band splitting, although the large gap might bring difficulty unless charge carriers are doped into the system, and thermal Hall measurements if the Néel vector orientation can be adjusted. The layered crystal structure of $La_2O_3Mn_2Se_2$ and the compositional flexibility of its analogs provides a fertile ground for new altermagnet search and optimization in strongly correlated materials.

ACKNOWLEDGMENTS

We thank I. Mazin for the fruitful discussions. C.-C.W. and H.J. are supported by an NSF Career Grant No. 2145832. X.L. and F.L. acknowledge financial support from the DOE-BES (Grant No. DE-FG02-04ER46148). Computational resources for this work were supported by CHPC of the University of Utah and the DOE-NERSC. The atomic and magnetic pair distribution function analysis performed by S.R.H. and B.A.F. was supported by the U.S. Department of Energy, Office of Science, Basic Energy Sciences (DOE-BES) through Award No. DE-SC0021134. The neutron scattering experiments used resources at the Spallation Neutron Source, a DOE Office of Science User Facility operated by the Oak Ridge National Laboratory. X.H. and T.T.T. thank the NSF (Awards No. NSF-OIA-2227933 and No. NSF-DMR-2338014) and the Arnold and Mabel Backman Foundation (2023 BYI Grant) for the support. The Air Force Office of Scientific Research supported R.M.F. (phenomenological model) under Award No. FA9550-21-1–0423 as well as B.S., K.M.K., and K.S.B. (Raman measurements and analysis) under Award No. FA9550-24-1–0110. L.Z. acknowledges the support by the NSF CAREER Grant No. DMR-174774 and Alfred P. Sloan Foundation.

[1] Y. Huai, F. Albert, P. Nguyen, M. Pakala, and T. Valet, Observation of spin-transfer switching in deep submicron-sized and low-resistance magnetic tunnel junctions, Appl. Phys. Lett. **84**, 3118 (2004).

[2] T. Miyazaki and N. Tezuka, Giant magnetic tunneling effect in Fe/Al_2O_3/Fe junction, J. Magn. Magn. Mater. **139**, L231 (1995).

[3] R. Cheng, M. W. Daniels, J.-G. Zhu, and D. Xiao, Ultrafast switching of antiferromagnets via spin-transfer torque, Phys. Rev. B **91**, 064423 (2015).

[4] N. L. Nair, E. Maniv, C. John, S. Doyle, J. Orenstein, and J. G. Analytis, Electrical switching in a magnetically intercalated transition metal dichalcogenide, Nat. Mater. **19**, 153 (2020).

[5] P. Wadley, B. Howells, J. Železný, C. Andrews, V. Hills, R. P. Campion, V. Novák, K. Olejník, F. Maccherozzi, S. S. Dhesi *et al.*, Electrical switching of an antiferromagnet, Science **351**, 587 (2016).

[6] S. Y. Bodnar, L. Šmejkal, I. Turek, T. Jungwirth, O. Gomonay, J. Sinova, A. A. Sapozhnik, H. J. Elmers, M. Kläui, and M. Jourdan, Writing and reading antiferromagnetic Mn_2Au by

Néel spin-orbit torques and large anisotropic magnetoresistance, Nat. Commun. **9**, 348 (2018).

[7] K. Ishizaka, M. S. Bahramy, H. Murakawa, M. Sakano, T. Shimojima, T. Sonobe, K. Koizumi, S. Shin, H. Miyahara, A. Kimura *et al.*, Giant Rashba-type spin splitting in bulk BiTeI, Nat. Mater. **10**, 521 (2011).

[8] J. Železný, H. Gao, K. Výborný, J. Zemen, J. Mašek, A. Manchon, J. Wunderlich, J. Sinova, and T. Jungwirth, Relativistic Néel-order fields induced by electrical current in antiferromagnets, Phys. Rev. Lett. **113**, 157201 (2014).

[9] X. Zhang, Q. Liu, J.-W. Luo, A. J. Freeman, and A. Zunger, Hidden spin polarization in inversion-symmetric bulk crystals, Nat. Phys. **10**, 387 (2014).

[10] L. Šmejkal, J. Sinova, and T. Jungwirth, Emerging research landscape of altermagnetism, Phys. Rev. X **12**, 040501 (2022).

[11] L. Šmejkal, R. González-Hernández, T. Jungwirth, and J. Sinova, Crystal time-reversal symmetry breaking and spontaneous Hall effect in collinear antiferromagnets, Sci. Adv. **6**, eaaz8809 (2020).

[12] L. Šmejkal, J. Sinova, and T. Jungwirth, Beyond conventional ferromagnetism and antiferromagnetism: A phase with nonrelativistic spin and crystal rotation symmetry, Phys. Rev. X **12**, 031042 (2022).

[13] L.-D. Yuan, Z. Wang, J.-W. Luo, E. I. Rashba, and A. Zunger, Giant momentum-dependent spin splitting in centrosymmetric low-*Z* antiferromagnets, Phys. Rev. B **102**, 014422 (2020).

[14] S. Hayami, Y. Yanagi, and H. Kusunose, Momentum-dependent spin splitting by collinear antiferromagnetic ordering, J. Phys. Soc. Jpn. **88**, 123702 (2019).

[15] R. D. Gonzalez Betancourt, J. Zubáč, R. Gonzalez-Hernandez, K. Geishendorf, Z. Šobáň, G. Springholz, K. Olejník, L. Šmejkal, J. Sinova, T. Jungwirth, S. T. B. Goennenwein, A. Thomas, H. Reichlová, J. Železný, and D. Kriegner, Spontaneous anomalous Hall effect arising from an unconventional compensated magnetic phase in a semiconductor, Phys. Rev. Lett. **130**, 036702 (2023).

[16] Z. Feng, X. Zhou, L. Šmejkal, L. Wu, Z. Zhu, H. Guo, R. González-Hernández, X. Wang, H. Yan, P. Qin *et al.*, An anomalous Hall effect in altermagnetic ruthenium dioxide, Nat. Electron. **5**, 735 (2022).

[17] R. González-Hernández, L. Šmejkal, K. Výborný, Y. Yahagi, J. Sinova, T. Jungwirth, and J. Železný, Efficient electrical spin splitter based on nonrelativistic collinear antiferromagnetism, Phys. Rev. Lett. **126**, 127701 (2021).

[18] S. Karube, T. Tanaka, D. Sugawara, N. Kadoguchi, M. Kohda, and J. Nitta, Observation of spin-splitter torque in collinear antiferromagnetic RuO_2, Phys. Rev. Lett. **129**, 137201 (2022).

[19] L. Šmejkal, A. B. Hellenes, R. González-Hernández, J. Sinova, and T. Jungwirth, Giant and tunneling magnetoresistance in unconventional collinear antiferromagnets with nonrelativistic spin-momentum coupling, Phys. Rev. X **12**, 011028 (2022).

[20] T. Jungwirth, R. Fernandes, J. Sinova, and L. Šmejkal, Altermagnets and beyond: Nodal magnetically-ordered phases, arXiv:2409.10034.

[21] I. I. Mazin, K. Koepernik, M. D. Johannes, R. González-Hernández, and L. Šmejkal, Prediction of unconventional magnetism in doped $FeSb_2$, Proc. Natl. Acad. Sci. USA **118**, e2108924118 (2021).

[22] Y. Guo, H. Liu, O. Janson, I. C. Fulga, J. van den Brink, and J. I. Facio, Spin-split collinear antiferromagnets: A large-scale *ab-initio* study, Mater. Today Phys. **32**, 100991 (2023).

[23] A. Smolyanyuk, L. Šmejkal, and I. Mazin, A tool to check whether a symmetry-compensated collinear magnetic material is antiferro- or altermagnetic, SciPost Phys. Codebases, 30 (2024).

[24] B. Jiang, M. Hu, J. Bai, Z. Song, C. Mu, G. Qu, W. Li, W. Zhu, H. Pi, Z. Wei *et al.*, Discovery of a metallic room-temperature d-wave altermagnet KV_2Se_2O, arXiv:2408.00320.

[25] H.-Y. Ma, M. Hu, N. Li, J. Liu, W. Yao, J.-F. Jia, and J. Liu, Multifunctional antiferromagnetic materials with giant piezomagnetism and noncollinear spin current, Nat. Commun. **12**, 2846 (2021).

[26] J. Krempaský, L. Šmejkal, S. W. D'Souza, M. Hajlaoui, G. Springholz, K. Uhlířová, F. Alarab, P. C. Constantinou, V. Strocov, D. Usanov *et al.*, Altermagnetic lifting of Kramers spin degeneracy, Nature (London) **626**, 517 (2024).

[27] C. Li, M. Hu, Z. Li, Y. Wang, W. Chen, T. Balasubramanian, M. Leandersson, C. Polley, T. Kim, H. Liu *et al.*, Topological Weyl altermagnetism in CrSb, arXiv:2405.14777.

[28] J. Ma, Z. Lin, D. Chen, W. Lu, X. Liang, S. Feng, K. Yamagami, J. Osiecki, M. Leandersson, T. Balasubramanian *et al.*, Observation of giant spin splitting and d-wave spin texture in room temperature altermagnet RuO_2, arXiv:2402.04995.

[29] P. Keßler, L. Garcia-Gassull, A. Suter, T. Prokscha, Z. Salman, D. Khalyavin, P. Manuel, F. Orlandi, I. Mazin, R. Valentı, and S. Moser, Absence of magnetic order in RuO_2: Insights from μSR spectroscopy and neutron diffraction, npj Spintron. **2**, 50 (2024).

[30] S. G. Jeong, I. H. Choi, S. Nair, L. Buiarelli, B. Pourbahari, J. Y. Oh, N. D. Bassim, A. Seo, W. S. Choi, R. M. Fernandes *et al.*, Altermagnetic polar metallic phase in ultra-thin epitaxially-strained RuO_2 films, arXiv:2405.05838.

[31] M. Hiraishi, H. Okabe, A. Koda, R. Kadono, T. Muroi, D. Hirai, and Z. Hiroi, Nonmagnetic ground state in RuO_2 revealed by muon spin rotation, Phys. Rev. Lett. **132**, 166702 (2024).

[32] O. Fedchenko, J. Minár, A. Akashdeep, S. W. D'Souza, D. Vasilyev, O. Tkach, L. Odenbreit, Q. Nguyen, D. Kutnyakhov, N. Wind *et al.*, Observation of time-reversal symmetry breaking in the band structure of altermagnetic RuO_2, Sci. Adv. **10**, eadj4883 (2024).

[33] J. M. Mayer, L. F. Schneemeyer, T. Siegrist, J. V. Waszczak, and B. Van Dover, New layered iron-lanthanum-oxide-sulfide and -selenide phases: $Fe_2La_2O_3E_2$(E = S,Se), Angew. Chem. Int. Ed. Engl. **31**, 1645 (1992).

[34] J.-X. Zhu, R. Yu, H. Wang, L. L. Zhao, M. D. Jones, J. Dai, E. Abrahams, E. Morosan, M. Fang, and Q. Si, Band narrowing and mott localization in iron oxychalcogenides $La_2O_2Fe_2O(Se, S)_2$, Phys. Rev. Lett. **104**, 216405 (2010).

[35] C. Wang, M.-q. Tan, C.-m. Feng, Z.-f. Ma, S. Jiang, Z.-a. Xu, G.-h. Cao, K. Matsubayashi, and Y. Uwatoko, $La_2Co_2Se_2O_3$: A quasi-two-dimensional Mott insulator with unusual cobalt spin state and possible orbital ordering, J. Am. Chem. Soc. **132**, 7069 (2010).

[36] Y. Fuwa, M. Wakeshima, and Y. Hinatsu, Crystal structure, magnetic properties, and Mössbauer spectroscopy of new layered iron oxyselenide $Nd_2Fe_2O_3Se_2$, J. Phys. Condens. Matter **22**, 346003 (2010).

[37] M. Rotter, M. Tegel, and D. Johrendt, Superconductivity at 38 K in the iron arsenide $(Ba_{1-x}K_x)Fe_2As_2$, Phys. Rev. Lett. **101**, 107006 (2008).

[38] D. Hirai, F. von Rohr, and R. J. Cava, Emergence of superconductivity in $BaNi_2(Ge_{1-x}P_x)_2$ at a structural instability, Phys. Rev. B **86**, 100505(R) (2012).

[39] H. Mizoguchi, T. Kuroda, T. Kamiya, and H. Hosono, $LaCo_2B_2$: A Co-based layered superconductor with a $ThCr_2Si_2$-type structure, Phys. Rev. Lett. **106**, 237001 (2011).

[40] R. M. Fernandes, A. I. Coldea, H. Ding, I. R. Fisher, P. J. Hirschfeld, and G. Kotliar, Iron pnictides and chalcogenides: A new paradigm for superconductivity, Nature (London) **601**, 35 (2022).

[41] D. S. Antonenko, R. M. Fernandes, and J. W. F. Venderbos, Mirror Chern bands and Weyl nodal loops in altermagnets, arXiv:2402.10201.

[42] I. Mazin, R. Gonzalez-Hernandez, and L. Šmejkal, Induced monolayer altermagnetism in $MnP(S, Se)_3$ and FeSe, arXiv:2309.02355.

[43] B. Brekke, A. Brataas, and A. Sudbø, Two-dimensional altermagnets: Superconductivity in a minimal microscopic model, Phys. Rev. B **108**, 224421 (2023).

[44] G. Giovannetti, L. de' Medici, M. Aichhorn, and M. Capone, $La_2O_3Fe_2Se_2$: A Mott insulator on the brink of orbital-selective metallization, Phys. Rev. B **91**, 085124 (2015).

[45] G. Wang, M. Zhang, L. Zheng, and Z. Yang, Orbital ordering in Mott-insulators $La_2O_3Fe_2Se_2$ and $La_2O_3Co_2Se_2$, Solid State Commun. **151**, 1231 (2011).

[46] L.-D. Yuan and A. Zunger, Degeneracy removal of spin bands in collinear antiferromagnets with non-interconvertible spin-structure motif pair, Adv. Mater. **35**, 2211966 (2023).

[47] N. Ni, E. Climent-Pascual, S. Jia, Q. Huang, and R. J. Cava, Physical properties and magnetic structure of the layered oxyselenide $La_2O_3Mn_2Se_2$, Phys. Rev. B **82**, 214419 (2010).

[48] E. Takeshi and S. J. L. Billinge, *Underneath the Bragg Peaks,* Pergamon Materials Series (Pergamon Press, London, 2012).

[49] B. Frandsen, X. Yang, and S. Billinge, Magnetic pair distribution function analysis of local magnetic correlations, Acta Crystallogr. Sect. A **70**, 3 (2013).

[50] B. Frandsen and S. Billinge, Magnetic structure determination from the magnetic pair distribution function (mPDF): Ground state of MnO, Acta Crystallogr. Sect. A **71**, 325 (2015).

[51] P. Juhás, Christopher L. Farrow, X. Yang, K. R. Knox, and S. J. L. Billinge, Complex modeling: A strategy and software program for combining multiple information sources to solve ill posed structure and nanostructure inverse problems, Acta Crystallogr. Sect. A **71**, 562 (2015).

[52] B. A. Frandsen, P. K. Hamilton, J. A. Christensen, E. Stubben, and S. J. L. Billinge, diffpy.mpdf: Open-source software for magnetic pair distribution function analysis, J. Appl. Crystallogr. **55**, 1377 (2022).

[53] G. Kresse and J. Furthmüller, Efficient iterative schemes for *ab initio* total-energy calculations using a plane-wave basis set, Phys. Rev. B **54**, 11169 (1996).

[54] P. E. Blöchl, Projector augmented-wave method, Phys. Rev. B **50**, 17953 (1994).

[55] J. P. Perdew, K. Burke, and M. Ernzerhof, Generalized gradient approximation made simple, Phys. Rev. Lett. **77**, 3865 (1996).

[56] H. J. Monkhorst and J. D. Pack, Special points for Brillouin-zone integrations, Phys. Rev. B **13**, 5188 (1976).

[57] S. L. Dudarev, G. A. Botton, S. Y. Savrasov, C. J. Humphreys, and A. P. Sutton, Electron-energy-loss spectra and the structural stability of nickel oxide: An LSDA+U study, Phys. Rev. B **57**, 1505 (1998).

[58] Z. Fang, I. V. Solovyev, H. Sawada, and K. Terakura, First-principles study on electronic structures and phase stability of MnO and FeO under high pressure, Phys. Rev. B **59**, 762 (1999).

[59] D. G. Free, N. D. Withers, P. J. Hickey, and J. S. O. Evans, Synthesis, structure and properties of several new oxychalcogenide materials with the general formula $A_2O_2M_2OSe_2$ (A = La−Sm, M = Fe, Mn), Chem. Mater. **23**, 1625 (2011).

[60] M. J. Gray, N. Kumar, R. O'Connor, M. Hoek, E. Sheridan, M. C. Doyle, M. L. Romanelli, G. B. Osterhoudt, Y. Wang, V. Plisson *et al.*, A cleanroom in a glovebox, Rev. Sci. Instrum. **91**, 073909 (2020).

[61] Y. Tian, A. A. Reijnders, G. B. Osterhoudt, I. Valmianski, J. G. Ramirez, C. Urban, R. Zhong, J. Schneeloch, G. Gu, I. Henslee, and K. S. Burch, Low vibration high numerical aperture automated variable temperature Raman microscope, Rev. Sci. Instrum. **87**, 043105 (2016).

[62] D. G. Free and J. S. O. Evans, Low-temperature nuclear and magnetic structures of $La_2O_2Fe_2OSe_2$ from x-ray and neutron diffraction measurements, Phys. Rev. B **81**, 214433 (2010).

[63] Y. Fuwa, T. Endo, M. Wakeshima, Y. Hinatsu, and K. Ohoyama, Orthogonal spin arrangement in quasi-two-dimensional $La_2Co_2O_3Se_2$, J. Am. Chem. Soc. **132**, 18020 (2010).

[64] See Supplemental Material at http://link.aps.org/supplemental/10.1103/PhysRevMaterials.9.024402 for the band structure of LOMSO under various effective U parameters without SOC when assuming a G-type compensated magnetic state; the computied energies based on different magnetic states using GGA/LDA+U and various effecctive U parameters; and the band structure of LOMSO under various effective U parameters without SOC when assuming a non-magnetic state.

[65] R. M. Fernandes, V. S. de Carvalho, T. Birol, and R. G. Pereira, Topological transition from nodal to nodeless Zeeman splitting in altermagnets, Phys. Rev. B **109**, 024404 (2024).

[66] L. Ghivelder, I. Abrego Castillo, M. A. Gusmão, J. A. Alonso, and L. F. Cohen, Specific heat and magnetic order in $LaMnO_{3+\delta}$, Phys. Rev. B **60**, 12184 (1999).

[67] H. Takagi, R. Takagi, S. Minami, T. Nomoto, K. Ohishi, M. T. Suzuki, Y. Yanagi, M. Hirayama, N. D. Khanh, K. Karube *et al.*, Spontaneous topological Hall effect induced by non-coplanar antiferromagnetic order in intercalated van der Waals materials, Nat. Phys. **19**, 961 (2023).

[68] N. J. Ghimire, A. S. Botana, J. S. Jiang, J. Zhang, Y. S. Chen, and J. F. Mitchell, Large anomalous Hall effect in the chiral-lattice antiferromagnet $CoNb_3S_6$, Nat. Commun. **9**, 3280 (2018).

[69] H. Lei, E. S. Bozin, A. Llobet, V. Ivanovski, V. Koteski, J. Belosevic-Cavor, B. Cekic, and C. Petrovic, Magnetism in $La_2O_3(Fe_{1-x}Mn_x)_2Se_2$ tuned by Fe/Mn ratio, Phys. Rev. B **86**, 125122 (2012).

[70] Y. Yang, F. Yu, X. Wen, Z. Gui, Y. Zhang, F. Zhan, R. Wang, J. Ying, and X. Chen, Pressure-induced transition from a Mott insulator to a ferromagnetic Weyl metal in $La_2O_3Fe_2Se_2$, Nat. Commun. **14**, 2260 (2023).

[71] A. J. Jacobson and B. E. F. Fender, Covalency Parameters in MnSe and $MnSe_2$, J. Chem. Phys. **52**, 4563 (1970).

[72] S. Landsgesell, K. Prokeš, T. Hansen, and M. Frontzek, An unexpected gap: Magnetic structures of $La_2O_3(Fe_{1-x}Mn_x)_2Se_2$ investigated by neutron diffraction and physical property measurements, Acta Mater. **66**, 232 (2014).

[73] Y. Wang, G. B. Osterhoudt, Y. Tian, P. Lampen-Kelley, A. Banerjee, T. Goldstein, J. Yan, J. Knolle, H. Ji, R. J. Cava *et al.*, The range of non-Kitaev terms and fractional particles in α-$RuCl_3$, npj Quantum Mater. **5**, 14 (2020).

[74] P. Lemmens, G. Güntherodt, and C. Gros, Magnetic light scattering in low-dimensional quantum spin systems, Phys. Rep. **375**, 1 (2003).

[75] L. Šmejkal, A. H. MacDonald, J. Sinova, S. Nakatsuji, and T. Jungwirth, Anomalous Hall antiferromagnets, Nat. Rev. Mater. **7**, 482 (2022).

[76] R. Hoyer, R. Jaeschke-Ubiergo, K.-H. Ahn, L. Šmejkal, and A. Mook, Spontaneous crystal thermal Hall effect in insulating altermagnets, arXiv:2405.05090.

[77] Y. Singh, M. A. Green, Q. Huang, A. Kreyssig, R. J. McQueeney, D. C. Johnston, and A. I. Goldman, Magnetic order in $BaMn_2As_2$ from neutron diffraction measurements, Phys. Rev. B **80**, 100403(R) (2009).

Correction: The middle initial in the twelfth author's name was incorrect and has been fixed.